Available online at www.sciencedirect.com

SciVerse ScienceDirect

Procedia IUTAM 00 (2013) 000–000

Procedia IUTAM

www.elsevier.com/locate/procedia

Nonlinear Interfacial Wave Phenomena from the Micro- to the Macro-Scale

Dependence of time-periodic vortex sheets with surface tension on mean vortex sheet strength

David M. Ambrose[a,*], Jon Wilkening[b]

[a]*Department of Mathematics, Drexel University, Philadelphia, PA 19104, USA*
[b]*Department of Mathematics, University of California, Berkeley, CA 94720, USA*

Abstract

In recent work, the authors have computed time-periodic solutions of the vortex sheet with surface tension in the spatially periodic setting. In these prior results, the mean vortex sheet strength was taken to be zero, so that there is no net shear across the fluid interface. In the present contribution, we explore the effect of allowing such a net shear, finding time-periodic vortex sheets that overturn without rolling up. We also find that resonances between Fourier modes lead to disconnections in the bifurcation curves that describe a two-parameter family of time-periodic solutions.
© 2013 The Authors. Published by Elsevier B.V.
Selection and peer-review under responsibility of Cyprus University of Technology.

Keywords: bifurcation; fluid interface; standing waves; surface tension

1. Introduction

We consider the case of two immiscible fluids separated by a sharp interface subject to surface tension. The motion of the fluids is governed by the irrotational, incompressible Euler equations, and thus the interface is a vortex sheet. The initial value problem for this situation is known to be well-posed[1,2], and an efficient numerical method for the solution of this initial value problem has been developed[3,4]. While several studies of standing gravity-driven water waves have been performed[5,6,7,8,9,10], little is known about time-periodic solutions of the two-fluid system. Such solutions are of interest as they provide examples of global solutions that exist for all time, without rolling up indefinitely or self-intersecting.

The authors have previously developed a computational method for finding time-periodic solutions of nonlinear systems of partial differential equations. This method has been applied to the Benjamin-Ono equation[11,12] and to the vortex sheet with surface tension in the case of zero mean vortex sheet strength[13]. In the present contribution, we describe the results of this method for time-periodic vortex sheets with surface tension in the case of non-zero mean vortex sheet strength.

The numerical method we use is an adjoint-based minimization method. That is, we define a functional that is identically zero for time-periodic solutions of the vortex sheet with surface tension, and which is positive for solutions

* Corresponding author. Tel.: +1-215-895-6247 ; fax: +1-215-895-1582.
E-mail address: ambrose@math.drexel.edu

2210-9838 © 2013 The Authors. Published by Elsevier B.V.
Selection and peer-review under responsibility of Cyprus University of Technology.

that are not time-periodic. We then seek zero minimizers of this functional by a quasi-Newton, gradient descent algorithm; details are provided below in Section 2. As we have mentioned, the authors have applied versions of this method previously[11,12,13]; also, the first author and collaborators have applied a version of the method for a simple, cubic model of the vortex sheet with surface tension[14]. The second author and collaborators have developed an alternative, trust-region algorithm for computing time-periodic solutions of the irrotational water wave that is faster due to greater opportunity for parallelism and re-use of data. For water waves, however, evaluating the evolution equations requires solving an integral equation, and detailed computations necessitate a faster algorithm[15,16]. In the present case, there is no corresponding integral equation to solve, and the quasi-Newton algorithm is sufficient.

2. Problem Formulation and Numerical Method

We denote the location of the interface as $(x(\alpha,t), y(\alpha,t))$, and we also will write $z = x + iy$. The curve is parameterized by a variable α, which is taken in the interval $[0, 2\pi)$, and t is time. We consider the periodic case, so that $z(\alpha + 2\pi, t) = z(\alpha, t) + 2\pi$, for all α and t. We take unit normal and tangent vectors at each point to be $\hat{\mathbf{n}}$ and $\hat{\mathbf{t}}$, respectively. The normal velocity of the fluid is continuous across the interface, while there is a jump in the tangential velocity. The jump in pressure across the interface is $\tau\kappa$, where τ is the constant, positive coefficient of surface tension and κ is the curvature of the interface (this is the Laplace-Young boundary condition). We describe the motion of the interface as $(x,y)_t = U\hat{\mathbf{n}} + V\hat{\mathbf{t}}$. The tangent angle the interface forms with the horizontal is denoted by θ and the arclength from a fixed point is s; these are defined through the relations $\theta = \tan^{-1}(y_\alpha/x_\alpha)$ and $s_\alpha^2 = x_\alpha^2 + y_\alpha^2$. The vortex sheet strength, which is equal to the jump in tangential velocity across the interface, is denoted by γ. Following Hou, Lowengrub, and Shelley[3,4], we evolve θ rather than the Cartesian coordinates of the interface; the curve can easily be reconstructed from θ. The evolution equations are then as follows:

$$\theta_t = \frac{U_\alpha + V\theta_\alpha}{s_\alpha}, \qquad \gamma_t = \tau\left(\frac{\theta_\alpha}{s_\alpha}\right)_\alpha + \left(\frac{(V - \mathbf{W}\cdot\hat{\mathbf{t}})\gamma}{s_\alpha}\right)_\alpha.$$

Note that the mean of γ_t is zero, and therefore the mean vortex sheet strength is conserved by the flow. No evolution equation is needed for s_α, since we use an arclength parameterization at all times,

$$s(\alpha,t) = \frac{\alpha L(t)}{2\pi}, \qquad s_\alpha = \frac{L}{2\pi},$$

and since, given θ associated to a 2π-periodic curve, the length of the curve, $L(t)$, can be determined from θ. The tangential velocity, V, is chosen to maintain this arclength parameterization[3,4], whereas the normal velocity, U, is determined by the fluid dynamics. The Birkhoff-Rott integral, $\mathbf{W} = (W_1, W_2)$ is given by

$$W_1 - iW_2 = \frac{1}{4\pi i}\mathrm{PV}\int_0^{2\pi} \gamma(\alpha')\cot\left(\frac{z(\alpha) - z(\alpha')}{2}\right) d\alpha'.$$

The normal velocity, U, is then given by $U = \mathbf{W}\cdot\hat{\mathbf{n}}$. Without loss of generality, we can take $\tau = 1$ (otherwise we could rescale γ to achieve $\tau = 1$)[13].

We use the usual notation for initial data, $\theta(\alpha,0) = \theta_0(\alpha)$ and $\gamma(\alpha,0) = \gamma_0(\alpha)$. The Fourier modes of the solution are written $\hat{\theta}_k(t)$, $\hat{\gamma}_k(t)$. As $\hat{\gamma}_0(t)$ is independent of time, we write $\hat{\gamma}_0$ for the mean vortex sheet strength. We also introduce the notation $\mathbf{q}(\alpha,t) = (\theta(\alpha,t), \gamma(\alpha,t))$ and $\mathbf{q}_0 = (\theta_0, \gamma_0)$.

The main idea of the method developed by the authors for finding time-periodic solutions of nonlinear systems of partial differential equations is to seek solutions that minimize the functional

$$G_0(\mathbf{q}_0, T) = \int_0^{2\pi} |\mathbf{q}(\alpha,T) - \mathbf{q}_0(\alpha)|^2 \, d\alpha. \tag{1}$$

Clearly, if $G_0(\mathbf{q}_0, T) = 0$, then the solution with initial data $\mathbf{q}_0$ is time-periodic with period T. In previous work[13], the authors considered symmetric, time-periodic solutions of the vortex sheet with surface tension that alternately pass through a flat state of maximal kinetic energy and a rest state in which all the energy is stored as potential energy in

the interface. A factor of four in computational savings was achieved by requiring that $\theta_0 \equiv 0$ and minimizing the modified functional

$$G_1(\mathbf{q}_0, T) = \frac{1}{2}\int_0^{2\pi} |\gamma(\alpha, T/4)|^2 \, d\alpha. \tag{2}$$

A symmetry argument was used to show that $G_0 = 0$ whenever $\theta_0 \equiv 0$ and $G_1 = 0$. In the present setting, when the mean vortex sheet strength, $\hat{\gamma}_0$, is non-zero, the fluid will never completely come to rest and minimizing G_1 does not imply that $G_0 = 0$. However, we are able to find a new functional that also achieves the factor of four in speed without requiring $\hat{\gamma}_0 = 0$. Specifically, we continue to assume $\theta_0 \equiv 0$ and instead minimize

$$G(\mathbf{q}_0, T) = \frac{1}{8}\int_0^{2\pi} \left[\theta\left(\alpha, \frac{T}{4}\right) + \theta\left(\alpha - \pi, \frac{T}{4}\right)\right]^2 + \left[\gamma\left(\alpha, \frac{T}{4}\right) - \gamma\left(\alpha - \pi, \frac{T}{4}\right)\right]^2 \, d\alpha. \tag{3}$$

We claim that if γ_0 and T are found such that $G((0, \gamma_0), T) = 0$, then $G_0((0, \gamma_0), T) = 0$ and the solution is time-periodic. Indeed, suppose θ and γ are the corresponding solutions for which $G = 0$. Since γ and θ solve the evolution equations over $0 \le t \le \frac{T}{4}$, so do $\Gamma(\alpha, t) = \gamma(\alpha - \pi, \frac{T}{4} - t)$ and $\Theta(\alpha, t) = -\theta(\alpha - \pi, \frac{T}{4} - t)$. Since $G = 0$, we have $\gamma(\alpha, \frac{T}{4}) = \Gamma(\alpha, 0)$ and $\theta(\alpha, \frac{T}{4}) = \Theta(\alpha, 0)$; this implies that Γ and Θ are a continuation of γ and θ; thus, for $\frac{T}{4} \le t \le \frac{T}{2}$, we have $\theta(\alpha, t) = -\theta(\alpha - \pi, \frac{T}{2} - t)$, and $\gamma(\alpha, t) = \gamma(\alpha - \pi, \frac{T}{2} - t)$. Similarly, for $\frac{T}{2} \le t \le T$ we can continue the solution by taking $\gamma(\alpha, t) = \gamma(\alpha - \pi, t - \frac{T}{2})$ and $\theta(\alpha, t) = \theta(\alpha - \pi, t - \frac{T}{2})$. We see then that $\theta(\alpha, T) = \theta(\alpha - \pi, \frac{T}{2}) = -\theta(\alpha, 0) = 0$, so $\theta(\alpha, T) = \theta_0(\alpha)$. Similarly, we have $\gamma(\alpha, T) = \gamma(\alpha - \pi, \frac{T}{2}) = \gamma(\alpha, 0)$.

The minimization of the functional, G, starts with an initial guess, and then proceeds by the BFGS minimization algorithm [17]. In order to use this method, we need to be able to calculate the value of G as well the derivatives of the functional G with respect to each of $\mathbf{q}_0$ and T. For a given $\mathbf{q}_0$ and T, we can evaluate $G(\mathbf{q}_0, T)$ by computationally solving the initial value problem (until time T) using the numerical method of Hou, Lowengrub, and Shelley [3,4]. Furthermore, it is completely straightforward to calculate the derivative of G with respect to T; we comment now on how to find the derivative with respect to the initial data.

For simplicity of presentation, we will calculate the variational derivative of G with respect to the full initial data $\mathbf{q}_0$, even though in the minimization method we only need the derivative with respect to γ_0. We begin by introducing the notation

$$\mathbf{Q}(\alpha, t) = \left(\frac{\theta(\alpha, t) + \theta(\alpha - \pi, t)}{2}, \frac{\gamma(\alpha, t) - \gamma(\alpha - \pi, t)}{2}\right)$$

and $\mathbf{q}_t = F(\mathbf{q})$. (The operator F can be inferred from the above evolution equations). The functional G is then

$$G(\mathbf{q}_0, T) = \frac{1}{2}\int_0^{2\pi} |\mathbf{Q}(\alpha, T/4)|^2 \, d\alpha,$$

and we seek to calculate $\frac{\delta G}{\delta \mathbf{q}_0}$. We begin by taking the variation of G to find

$$\dot{G}(\mathbf{q}_0, T) = \left.\frac{d}{d\varepsilon}\right|_{\varepsilon=0} G(\mathbf{q}_0 + \varepsilon\dot{\mathbf{q}}_0, T) = \int_0^{2\pi} \mathbf{Q}(\alpha, T/4) \cdot \dot{\mathbf{Q}}(\alpha, T/4) \, d\alpha. \tag{4}$$

By using the definition of $\mathbf{Q}$ and changing variables in the integral, we notice that we can write this as

$$\dot{G}(\mathbf{q}_0, T) = \int_0^{2\pi} \mathbf{Q}(\alpha, T/4) \cdot \dot{\mathbf{q}}(\alpha, T/4) \, d\alpha.$$

We want to write this as an inner product:

$$\dot{G} = \left\langle \frac{\delta G}{\delta \mathbf{q}_0}, \dot{\mathbf{q}}_0 \right\rangle.$$

We define an auxiliary function $\tilde{\mathbf{Q}}(\alpha, s)$, $s = T/4 - t$, that will satisfy $\tilde{\mathbf{Q}}(\alpha, T/4) = \frac{\delta G}{\delta \mathbf{q}_0}$. We assign the initial value $\tilde{\mathbf{Q}}(\alpha, 0) = \mathbf{Q}(\alpha, T/4)$ and ask that the inner product $\langle \tilde{\mathbf{Q}}(\cdot, T/4 - t), \dot{\mathbf{q}}(\cdot, t)\rangle$ be constant. Differentiating with respect to time, we see that this quantity will indeed be constant if we take $\tilde{\mathbf{Q}}$ to be the solution of the differential equation

$$\tilde{\mathbf{Q}}_s = (DF(\mathbf{q}(\cdot, T/4 - s)))^* \, \tilde{\mathbf{Q}},$$

with the previously given initial condition. The operator DF is the linearized evolution operator for the vortex sheet with surface tension, while $(DF)^*$ is its adjoint; both were calculated by the authors in previous work [13]. Thus, we see that evaluating the variational derivative, $\frac{\delta G}{\delta \mathbf{q}_0}$, requires the numerical solution of two initial value problems, one for $\mathbf{q}$ and one for $\tilde{\mathbf{Q}}$.

3. Numerical Results

Using this method, we calculate bifurcations from the flat equilibrium configuration of the vortex sheet with surface tension to genuinely time-periodic flows. The equilibrium solution is time-periodic for any period, so we first want to predict the period at which the bifurcation will occur by using linear theory. We begin by linearizing the evolution equations about $\theta(\alpha,t) = 0,\ \gamma(\alpha,t) = \hat{\gamma}_0$. Letting $\dot{\theta}$ and $\dot{\gamma}$ be the perturbations in θ and γ, respectively, the linearized equations are [4]

$$\dot{\theta}_t = \frac{1}{2} H\dot{\gamma}_\alpha, \qquad \dot{\gamma}_t = \dot{\theta}_{\alpha\alpha} + \frac{1}{2}\hat{\gamma}_0^2 H\dot{\theta}_\alpha,$$

where H is the Hilbert transform. For a given wave number $k > 0$, we can find time-periodic solutions of this linear equation as long as $\hat{\gamma}_0^2 < 2k$. Up to spatial and temporal phase shifts, they are given by the following formulas:

$$\dot{\theta} = A\sin(\omega_k t)\cos(k\alpha), \qquad \omega_k = \frac{1}{2}\sqrt{2k^3 - \hat{\gamma}_0^2 k^2}, \qquad \dot{\gamma} = B\cos(\omega_k t)\cos(k\alpha), \qquad A = \frac{k}{2\omega_k}B. \tag{5}$$

Thus, we expect bifurcation from the flat equilibrium solution to occur with periods $T_k = \frac{2\pi}{\omega_k} = \frac{4\pi}{\sqrt{2k^3 - \hat{\gamma}_0^2 k^2}}$.

As shown in Figure 1, this is indeed what we find. For simplicity, we restrict to the case $k = 1$. For 100 values of $\hat{\gamma}_0$ ranging from 0.01 to 1, we computed time-periodic solutions for 50 values of $\hat{\gamma}_1(0)$ ranging from -0.01 to -0.5. These two Fourier modes of the initial condition are used as bifurcation parameters. The BFGS algorithm minimizes $G((0,\gamma_0),T)$ in (3) by varying the remaining Fourier modes $\hat{\gamma}_k(0)$, $|k| \geq 2$, and the period, T. The starting guess (in the BFGS minimization) for the first two solutions on each curve were taken of the form (5) with $B = -0.02$ and $B = -0.04$, respectively. Subsequent starting guesses were obtained by linear extrapolation of the two previous solutions.

In Figures 2 and 3 we plot snapshots of the solutions labeled A, B, C in Figure 1. Solution A behaves similarly to standing waves of the linearized problem, with smooth, nearly sinusoidal waves growing and decaying in a regular

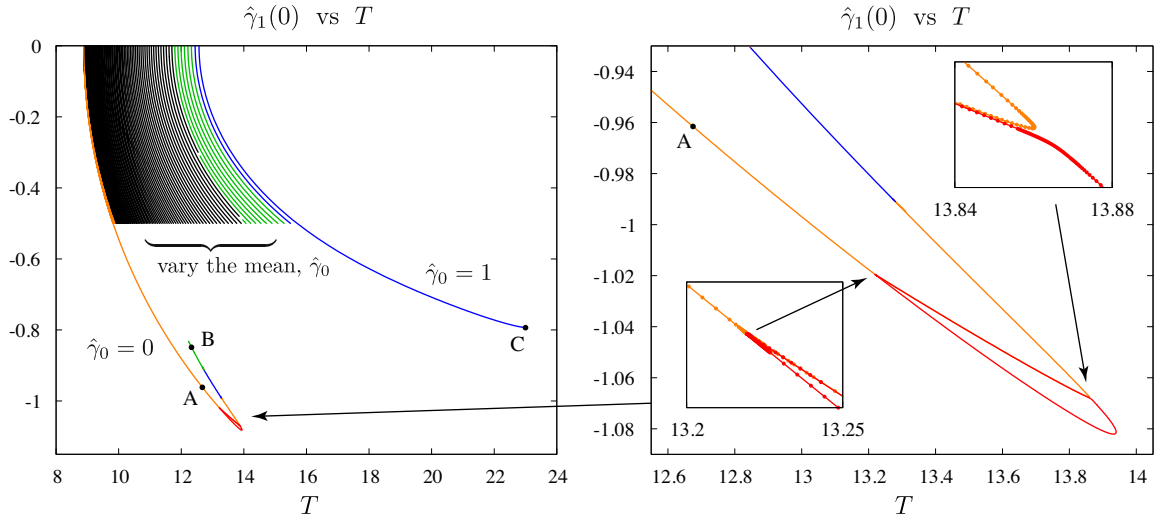

Fig. 1. (left) For each value of $\hat{\gamma}_0 \in \{0, 1, \ldots, 100\}/100$, the solution is continued from $\hat{\gamma}_1(0) = 0$ to $\hat{\gamma}_1(0) = -0.5$. The first and last curves are followed until further continuation becomes too expensive. The solutions labeled A, B and C are shown in Figures 2 and 3.; (right) A closer look at the $\hat{\gamma}_0 = 0$ curve, which was studied in detail in previous work [13], reveals disconnections due to nonlinear resonances.

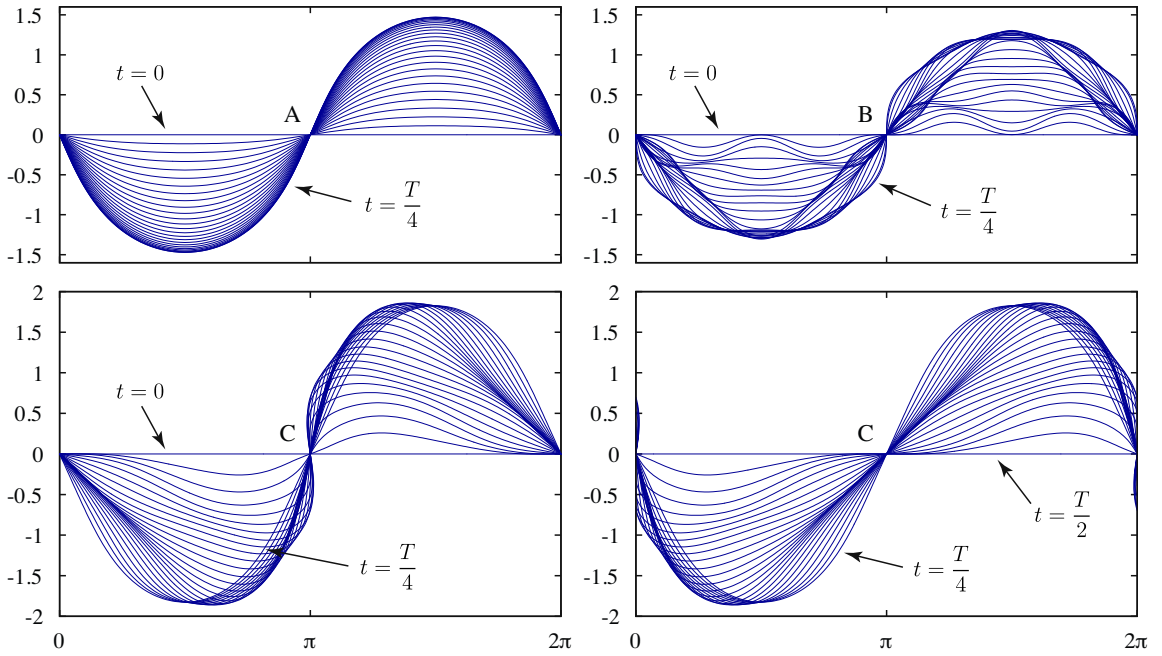

Fig. 2. Profiles of the solutions labeled A, B, and C in Figure 1. The solutions with mean-zero vortex sheet strength exhibit additional symmetries (with respect to both space and time) that are not present in the general case.

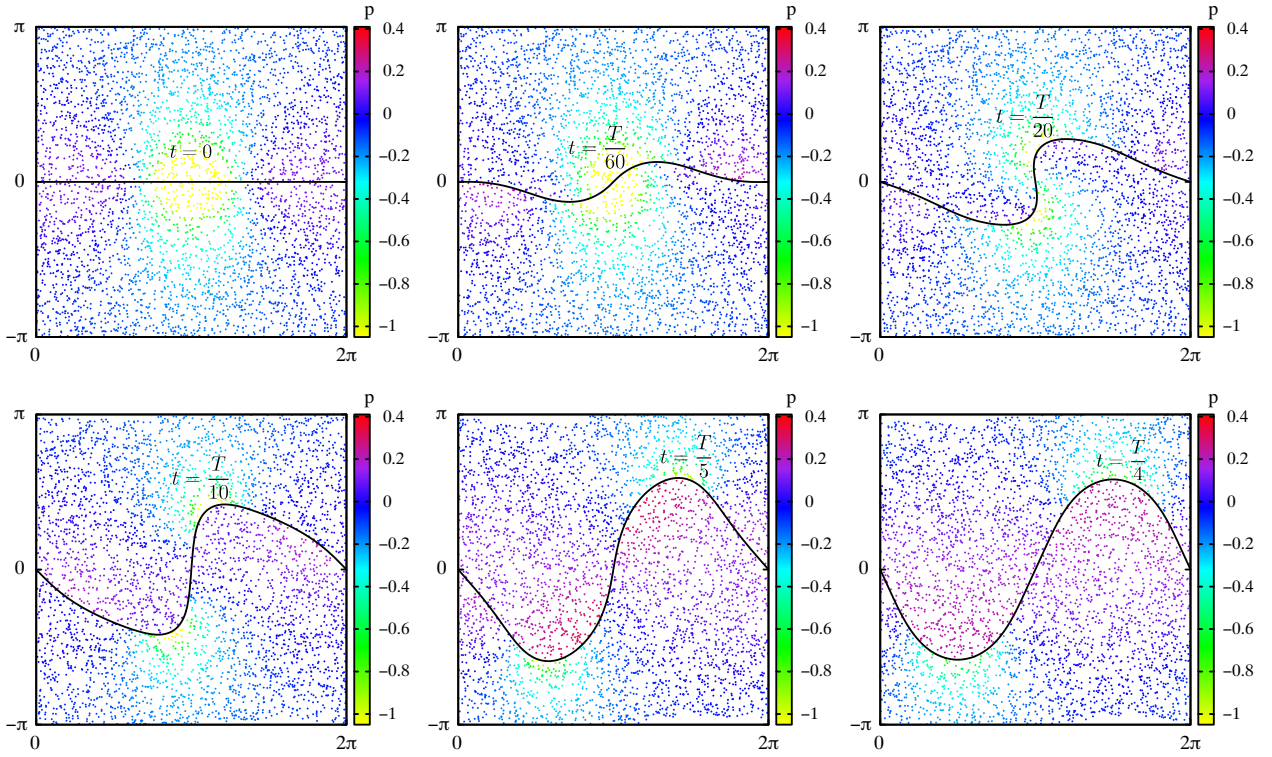

Fig. 3. The position of the vortex sheet labeled C in Figure 1 at various times during the evolution. The particles in the fluid regions are passive tracers added to help visualize the flow, with color-coded pressure. The interface overturns, but avoids completely rolling up, before evolving to its initial configuration again.

fashion. Solution B contains a strong secondary standing wave of shorter wavelength and faster frequency of oscillation superposed (nonlinearly) on top of the basic carrier wave. While it is difficult to ascribe a single wave number to the secondary wave since this resonance involves many modes interacting at finite amplitude, animations of this solution give the impression of a $k = 5$ mode oscillating 11 times per cycle of the $k = 1$ carrier mode. However, the oscillations of the $k = 5$ mode are not uniform in time, proceeding significantly faster near the flat state ($t = 0, T/2$) than near the maximally stretched rest state ($t = T/4, 3T/4$). Solution C has less symmetry than solutions A and B due to $\hat{\gamma}_0 \neq 0$. More specifically, the solution is no longer invariant under reflection across the lines $x = \pi/2$ and $x = 3\pi/2$. As with solution B, higher-frequency capillary waves are visibly active on the vortex sheet during the course of its evolution.

Figure 3 shows particle plots of solution C, where the particles are passively advected with the flow, color coded by pressure. Note the large pressure drop across the interface in regions of high curvature. Pressure was normalized to be zero at $y = \pm\infty$. Regions of low (i.e. negative) pressure generally correspond to faster-moving fluid particles. In particle-plot animations, the most striking difference between solution C and the other two solutions is that the fluid velocity in A and B decays rapidly to zero away from the vortex sheet while the x-component of velocity in solution C approaches $-1/2$ as $y \to \infty$ and $1/2$ as $y \to -\infty$. The amplitude of solution C is also somewhat larger, and its period is roughly twice as large as that of A or B. Solutions B and C both overturn (become multiple-valued) in the course of their evolution.

Of the 5000 solutions of the (numerically computed) two-parameter family in Figure 1, 50% of the solutions have $G < 10^{-29}$, 80% have $G < 10^{-25}$, 90% have $G < 10^{-22}$, and 98% have $G < 10^{-18}$. The vast majority of these could be improved to 10^{-29} by using more Fourier modes in the BFGS search and a finer mesh. However, two of the original 5000 solutions had $G > 10^{-15}$, namely $G = 1.3 \times 10^{-9}$ and $G = 8.1 \times 10^{-10}$. Even using extended precision arithmetic, it was not possible to reduce G further with these particular values of $\hat{\gamma}_0$ and $\hat{\gamma}_1(0)$.

The reason is that nonlinear resonances in the Fourier modes can leave gaps in the ranges of bifurcation parameters for which time-periodic solutions exist. As we numerically continue a path by varying $\hat{\gamma}_1(0)$ over a discrete set of values while holding $\hat{\gamma}_0$ fixed, the other Fourier modes (that minimize G) occasionally jump discontinuously. The dashed grey lines in Figure 4 are examples of such jumps that occur in the fourth Fourier mode.

We performed additional calculations with $\hat{\gamma}_0 \in \{0.01, \ldots, 0.15\}$ to fully resolve the first family of disconnections observed in this plot. The results, shown in Figures 5 and 6, reveal visible gaps in the allowed values of $\hat{\gamma}_1(0)$ and $\hat{\gamma}_2(0)$ for given values of $\hat{\gamma}_0$ due to resonances between the fourth and higher Fourier modes. We note that all the solutions of Figures 5 and 6 were computed to $G < 10^{-30}$, and many were computed to $G < 10^{-60}$ using 32 digits of precision in the numerical algorithm. Attempting to find solutions with bifurcation parameters in the gaps will lead to

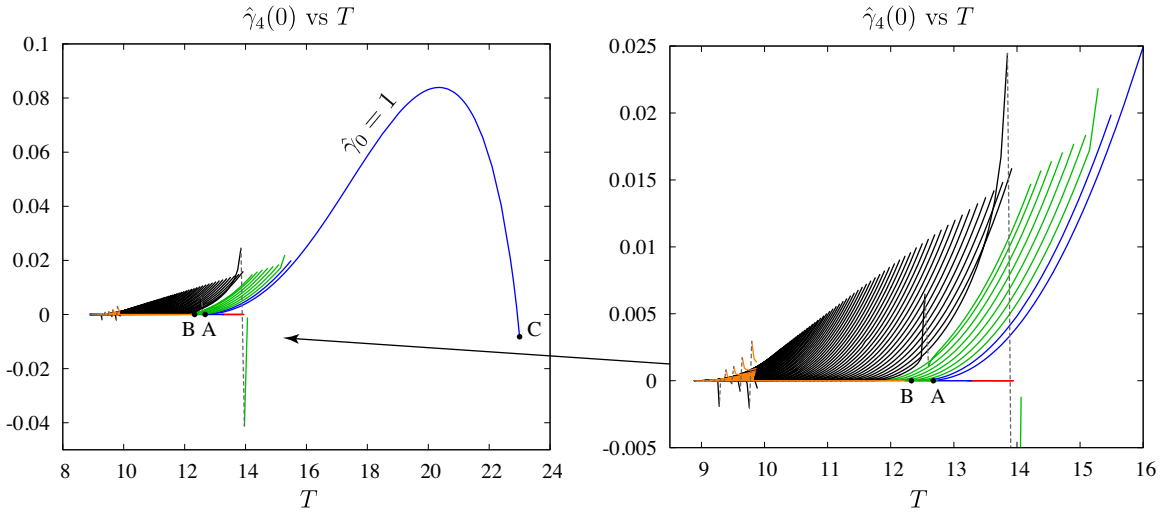

Fig. 4. (left) Disconnections propagate through the two-parameter family of solutions, and are more easily seen when higher Fourier modes (in this case, the fourth) are plotted. Different branches are colored differently.; (right) A detail from the figure on the left.

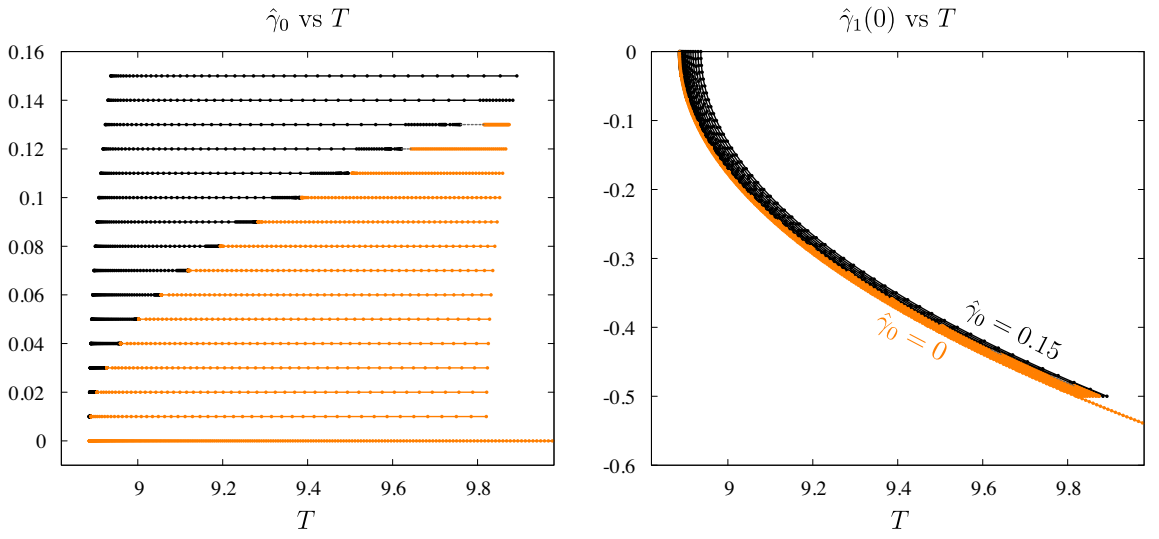

Fig. 5. (left) $\hat{\gamma}_0$ plotted versus the temporal period, T, for the recomputed solutions. The different colors on each horizontal segment reflects the presence of a disconnection.; (right) We recompute the first several curves from the left panel of Figure 1, to achieve higher resolution of the disconnections. These solutions all have $G < 10^{-30}$.

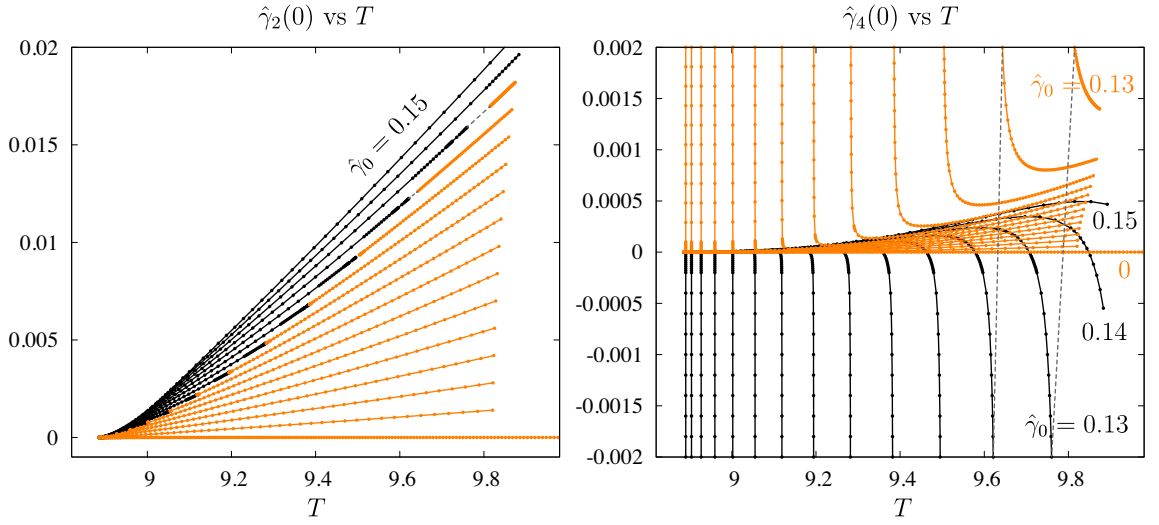

Fig. 6. (left) In this plot of $\hat{\gamma}_2(0)$ versus temporal period, T, for the recomputed, higher-precision solutions, gaps are noticeable. In two cases in the figure, we illustrate the gap with a dotted line.; (right) Rather than gaps, in this plot of $\hat{\gamma}_4(0)$ versus temporal period, T, for the recomputed, higher-precision solutions, jumps are evident. In two cases in the figure, we illustrate the jump with a dotted line.

G values that reach a non-zero local minimum. We generally reject solutions in which G cannot be made smaller than 10^{-25} with sufficient mesh refinement.

The solutions of Figures 5 and 6 were computed from the outside in, meaning that we used $\hat{\gamma}_4(0)$ as a bifurcation parameter to traverse the nearly vertical parts of the curves in the second panel of Figure 6, starting at the ends where $\hat{\gamma}_4(0) = \pm 0.002$ and following the curves back to the equilibrium solution by numerical continuation. Once the curves start to flatten, we switched back to $\hat{\gamma}_1(0)$ as the bifurcation parameter. The final stages of this procedure (near the equilibrium solution) were done using 32 digits of precision to avoid falling off the bifurcation curves. We note that the mean-zero solutions from previous work [13] are also plotted in these figures, but were not recomputed.

It is interesting that the disconnection shown in Figures 5 and 6 propagates all the way to the flat, rest state (with $\hat{\gamma}_0 = 0$). Thus, the branch of solutions obtained by first increasing $\hat{\gamma}_0$ and then increasing $\hat{\gamma}_1(0)$ is different than the

one obtained by performing the perturbations in the opposite order. We also note that many (perhaps infinitely many) additional disconnections are likely to run through this two-parameter family of solutions due to resonances in still higher Fourier modes. Such resonances are likely to be invisible to the first few modes in floating point arithmetic, but would have to be dealt with in a rigorous proof of existence of time-periodic vortex sheets.

Acknowledgements

DMA was supported by the National Science Foundation through grants DMS-1016267 and DMS-1008387. JW was supported through the National Science Foundation through grant DMS-0955078 and by the Director, Office of Science, Computational and Technology Research, US Department of Energy under Contract DE-AC02-05CH11231.

References

1. Ambrose, D.. Well-posedness of vortex sheets with surface tension. *SIAM J Math Anal* 2003;**35**:211–244.
2. Cheng, C.H., Coutand, D., Shkoller, S.. On the motion of vortex sheets with surface tension in three-dimensional Euler equations with vorticity. *Comm Pure Appl Math* 2008;**61**:1715–1752.
3. Hou, T., Lowengrub, J., Shelley, M.. Removing the stiffness from interfacial flows with surface tension. *J Comp Phys* 1994;**114**:312–338.
4. Hou, T., Lowengrub, J., Shelley, M.. The long-time motion of vortex sheets with surface tension. *Phys Fluids* 1997;**9**:1933–1954.
5. Penney, W.G., Price, A.T.. Finite periodic stationary gravity waves in a perfect liquid. *Phil Trans R Soc Lond A* 1952;**244**:254–284.
6. Tadjbakhsh, I., Keller, J.B.. Standing surface waves of finite amplitude. *J Fluid Mech* 1960;**8**:442–451.
7. Mercer, G.N., Roberts, A.J.. Standing waves in deep water: Their stability and extreme form. *Phys Fluids A* 1992;**4**(2):259–269.
8. Bryant, P.J., Stiassnie, M.. Different forms for nonlinear standing waves in deep water. *J Fluid Mech* 1994;**272**:135–156.
9. Okamura, M.. Standing gravity waves of large amplitude in deep water. *Wave Motion* 2003;**37**:173–182.
10. Iooss, G., Plotnikov, P., Toland, J.. Standing waves on an infinitely deep perfect fluid under gravity. *Arch Rat Mech Anal* 2005;**177**:367–478.
11. Ambrose, D., Wilkening, J.. Computation of time-periodic solutions of the Benjmain-Ono equation. *J Nonlinear Sci* 2010;**20**:277–308.
12. Ambrose, D., Wilkening, J.. Global paths of time-periodic solutions of the BenjaminOno equation connecting pairs of traveling waves. *Comm Appl Math and Computational Sci* 2009;**4**:177–215.
13. Ambrose, D., Wilkening, J.. Computation of symmetric, time-periodic solutions of the vortex sheet with surface tension. *Proc Nat Acad Sci USA* 2010;**107**:3361–3366.
14. Ambrose, D., Kondrla, M., Valle, M.. Computing time-periodic solutions of a model for the vortex sheet with surface tension. *Quart Appl Math* 2013;In press.
15. Wilkening, J.. Breakdown of self-similarity at the crests of large amplitude standing water waves. *Phys Rev Lett* 2011;**107**(184501).
16. Wilkening, J., Yu, J.. Overdetermined shooting methods for computing standing water waves with spectral accuracy,. *Comput Sci Disc* 2012;**5**(014017).
17. Nocedal, J., Wright, S.. *Numerical Optimization*. New York: Springer; 1999.